IEEE Open Journal of Power Electronics

Received XX Month, XXXX; revised XX Month, XXXX; accepted XX Month, XXXX; Date of publication XX Month, XXXX; date of current version XX Month, XXXX.

Digital Object Identifier 10.1109/OJPEL.2022.0817315

Multi-Source Dual Active Bridge DC/DC Converter for More Electric Aircraft

MOHAMED I. HASSAN[*], ***Student Member, IEEE***, **NILOUFAR KESHMIRI**[*], ***Student Member, IEEE***, **OMAR ZAYED**[†], ***Student Member, IEEE***, **MEHDI NARIMANI**[†], ***SENIOR MEMBER, IEEE***, **AND ALI EMADI.**[*], ***Fellow, IEEE***

[1]McMaster Automotive Resource Centre (MARC), McMaster University, Hamilton, ON L8P 0A6, Canada
[2]Electrical and Computer Engineering, McMaster University, Hamilton, ON L8S 4K1, Canada

CORRESPONDING AUTHOR: Mohamed I. Hassan (e-mail: ibrahm50@mcmaster.ca).

This research was undertaken in part, thanks to funding from Mitacs through the Mitacs Accelerate program and EATON Aerospace Group.

ABSTRACT The topology proposed in this paper aims for a multiple sources/loads integration to improve the power density of the electrical power distribution system (EPDS) of the more-electric aircraft (MEA) architecture. The different operating modes of the proposed topology add flexibility to the system enabling power flow between different sources, while controlling the power supplied to the low voltage (LV) network on the aircraft. Better system utilization is achieved as compared to conventional solutions. The system stability is improved considering that the multi-source DAB (MSDAB) topology can be configured to stabilize the high-voltage DC (HVDC) bus in case of voltage sag. A battery charging configuration utilizing the magnetizing inductance of the transformer is proposed and discussed as one of the operating modes of the converter. The power flow to the low-voltage bus network is controlled by phase shifting the gating signals between the two bridges. A design process using genetic algorithm (GA) optimization is introduced to optimally select the converter parameters to minimize the transformer RMS current. Simulation and experiments of the control schemes were performed to validate optimal operation of the proposed converter.

INDEX TERMS HVDC converters, energy storage, power system stability, genetic algorithm.

I. Introduction

THE key figures of modernized aircraft electrical power networks are the weight and size reduction as well as the system efficiency [1]. Power electronic converters are considered the building blocks of such modernized networks. The basic electric power distribution system (EPDS) aboard the aircraft is illustrated in Fig. 1 [2]. Several derivatives of the basic EPDS have been developed over the years with a dependency on the available power electronics and control technologies [3]. Efforts have been made in the design of compact, lightweight distribution systems while enhancing efficiency and increasing power handling capabilities. Electric power utilization has increased in modern MEA architectures to replace the traditional mechanical systems. Two main engines and an auxiliary power unit (APU) are connected to generators with AC/DC rectifiers connected at the output of the generators to supply the high voltage DC (HVDC) bus where solid-state power controllers (SSPCs)

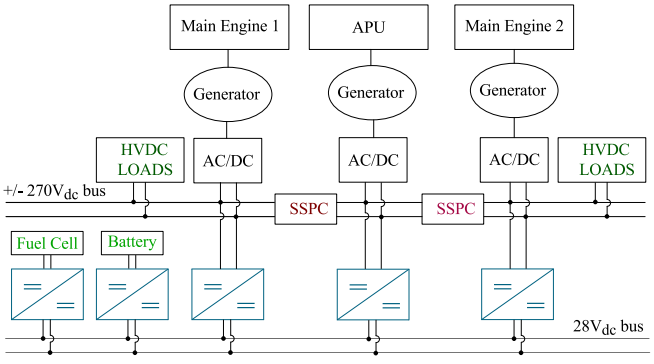

FIGURE 1. Generalized MEA electrical distribution system.

are used for protection. The HVDC link utilized in modern aircraft architectures provides an internal HVDC link that can be used for equipment such as radars and actuator controllers without the need for a conversion stage. The HVDC bus is then connected to a low voltage bus through multiple step-down isolated DC-DC converters. Other high-voltage DC loads are connected directly to the main HVDC bus.

The HVDC EPDS has been of interest among several research groups such as Airbus HVDC project [4], and CleanSky project [5]. The MEA EPDSs are the latest electrification level for commercial aircraft. Conventionally, a single-source DC/DC converter is used to link a power source such as the HVDC bus, batteries, and fuel cells to the low-voltage (28 V) DC network. The distribution system has to include auxiliary sources other than the main engines for emergency and ground operations. Multiple energy storage systems (ESSs) chemistries are utilized such as supercapacitors, batteries, and fuel cells. Each ESS chemistry provides benefits such as lower cost, faster response time, and higher performance. Some of the energy storage systems are connected to the low voltage network through isolated power converters. Conventionally, a kerosene-based APU (KB-APU) is utilized to provide emergency power. ESSs are used to provide power from the time the main engines fail till the activation of the KB-APU system. In case of failure of all systems including the KB-APU, ESSs have to supply the rated power for a short period of time. In compliance with the MIL-STD-704 standard, all power characteristics in emergency operation shall be the same as normal operation. Batteries and other independent ESSs should also be able to supply power for 30 minutes in an emergency state. Before the aircraft takes off, ground operation relies entirely on the KB-APU and ESSs when the main engines are shut off. The efficiency of a conventional KB-APU on the ground is very low which contributes the most to the emissions of airports. For the conventional systems, the ESSs are sized to supply power before the KB-APU takes over. This results in a very bulky system which forms 40% of the overall distribution system weight [6].

More electric technology can be achieved by replacing the traditional kerosene-operated turbine APU with a fuel cell system-based APU. This technology has been adopted recently due to strict emission regulations in airports while also promoting higher overall distribution system efficiency. Using fuel cells and batteries instead of or along with the KB-APU system reduces the system size required for ground and emergency operation. A more-electric configuration includes multiple energy sources/loads which calls for integration of the isolated DC-DC converters to improve the power density of the EPDS of the aircraft. Each section of the distribution system needs to be able to supply the peak power. The KB-APU along with the ESSs are sized to supply the rated power required in normal operation. This results in over-sizing the system since not all sources supply the peak power at the same time. Considering the conventional configuration of the EPDS, the isolated DC-DC converters are oversized.

Other architectures have been developed for improved integration of the different energy sources aboard the aircraft and the low-voltage network [7], [8]. A derivative of the architecture shown in Fig. 1 is the flexible modular power electronic converters (MPECs) architecture, where several isolated bidirectional DC/DC converters are connected in parallel [9]. Each low-power PEC is considered a bidirectional cell and can be connected to any of the main primary HVDC buses. The MPECs architecture provides flexibility and fault tolerance since all cells can operate in a modular parallel approach. The EPDS of the MPECs architecture can be considered as a micro-grid where an online supervisor controls the power flow of the modular converters. Control optimization of the modular converter can lead to a significant reduction in the system volume and weight. The MPEC approach allows for a reduction in the size of the isolated DC-DC converters supplying the LV network, since lower-power paralleled DC-DC converters are utilized with access to all HVDC links and battery/fuel cell terminals. The main supervisor is responsible for controlling the power flow between the paralleled converters.

A multi-source isolated DC/DC converter is proposed in this paper following the MPECs approach of paralleling multiple low-power modules. The multi-source topology allows for power flow between the different energy sources/DC links, which increases the stability of the system. This can be realized through a similar approach as the MPECs, by having multiple parallel multi-source isolated DC-DC converters where power flow between the input terminals can be controlled. The power can be supplied to the LV network through either of the connected sources or through splitting the power between the different sources. The proposed MSDAB topology is introduced in Section II based on the conventional DAB converter. The importance of multi-source integration is highlighted in this section. A design comparison to the conventional approach, considering the different modes of the MSDAB topology, is carried out. Section III discusses the mathematical modeling of the MSDAB topology based on a Fourier-transform approach. Furthermore, an optimization methodology is developed to optimize each mode of operation which includes two layers of optimization through a genetic algorithm (GA); layer 1: optimization of transformer turns ratio and DAB inductor, and layer 2: phase angle optimization by using triple phase shift (TPS) control for the DAB converter [10]–[12]. In Section IV, the experimental setup is shown, and key waveforms and efficiency plots are presented. The different modes of operations are tested highlighting the effect on the control flexibility and system stability. The developed GA algorithms are tested for the two main converter modes at different power and voltage operating points.

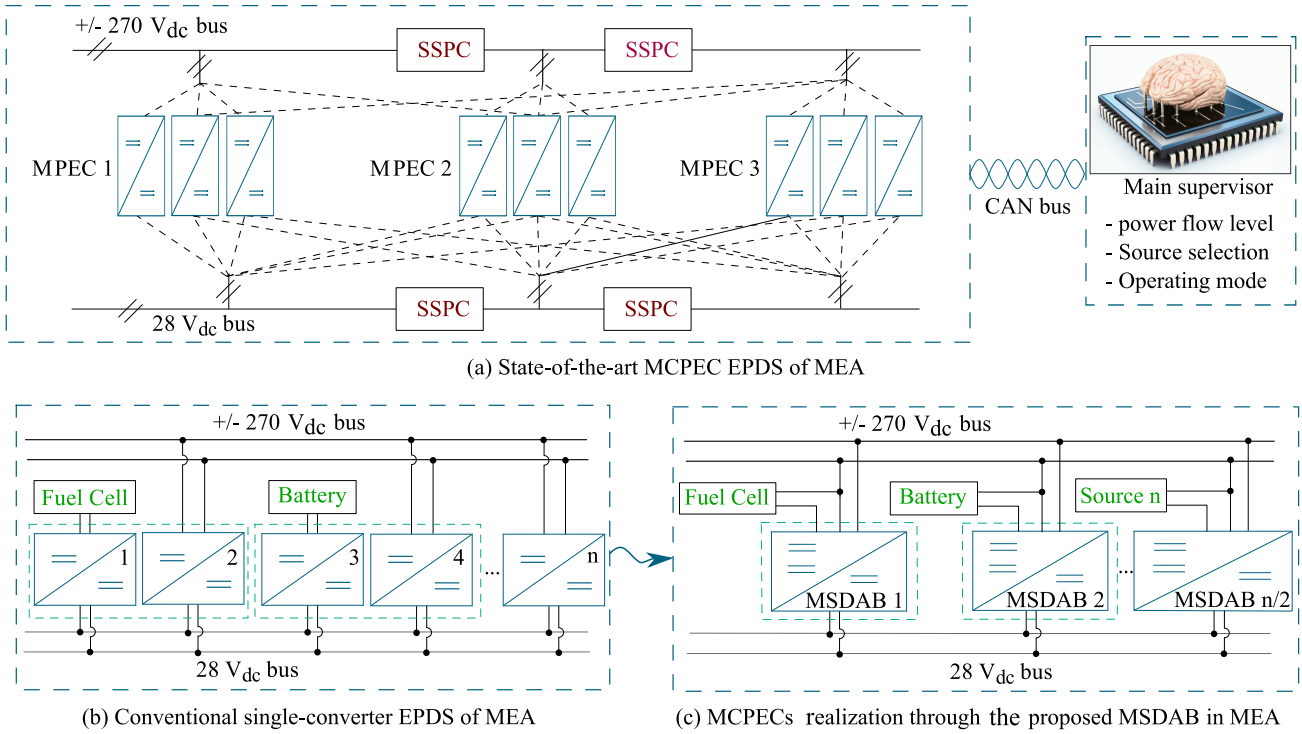

FIGURE 2. Different MEA electrical distribution system. (a) State-of-the-art MCPEC EPDS of MEA. (b) Conventional single-converter EPDS. (c) MPECs realization through the proposed MSDAB in MEA EPDS.

II. MPECs Approach and Proposed Multi-source DC-DC Converter

This section presents the realization of MPECs architecture through the proposed MSDAB topology. The different modes of operation are discussed and compared to the conventional architecture. Galvanic isolation has to be maintained between the HVDC buses and the LVDC (28 V) network following the MIL-STD-704 standard. However, the output of the main generators and APU are directly connected to either separate HVDC links or a single HVDC bus. SSPCs are used as electrical non-isolated power interrupters in case of faults. As stated in the MIL-STD-704, AC inputs cannot be paralleled; however, DC sources can be paralleled with blocking diodes added for protection. The developed architecture has to comply with the isolation and protection requirements stated in the MIL-STD-704 standard.

Better converters utilization can be achieved through several multi-source DC-DC converters connected in parallel. This allows for power flow between the different energy sources/DC links whilst supplying power to the LV bus, which increases the stability of the system in case of voltage sag in one of the energy sources. The power can be supplied to the LV network through either of the connected sources or through splitting the power between the different sources. The MPECs architecture is illustrated in Fig. 2 (a). Fig. 2 (c) shows the realization of the MPECs architecture with two input sources connected through the proposed MSDAB topology as compared to the conventional approach illustrated in 2 (b). The power can be shared between the different sources while maintaining galvanic isolation between the HV sources and the LV network. Compared to the conventional structure, shown in Fig. 2 (b), the number of converters (n) is halved in the case of utilizing MSDABs. The MSDAB topology allows for power flow between the different energy sources/DC links, which increases the stability of the system. This can be realized through a similar approach as the MPECs, by having multiple parallel multi-source isolated DC-DC converters where power flow between the input terminals can be controlled. The power can be supplied to the LV network through either of the connected sources or through splitting the power between the different sources.

In addition, the proposed MSDAB offers the ability to charge the battery during flight without the need of an additional buck converter which would be necessary in a conventional architecture.

In the conventional EPDS, the isolated DC/DC converters connected to each of the HVDC buses are sized at the full rated power. The multi-source topology allows for a system size reduction as compared to the conventional configuration since power is split between all the sources and not all sources are required to supply the full power at the same time. For instance, the auxiliary batteries mainly supply power in ground operation or during an emergency, but conventionally a full-power converter is connected to each of the sources even though at some point some of these converters are not operating. This results in poor system utilization, which can be improved if those different sources

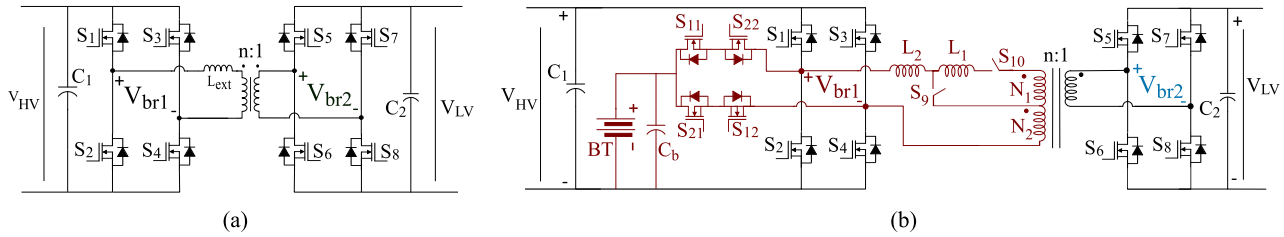

FIGURE 3. **Topological schematic comparison. (a) Conventional DAB schematic. (b) Proposed MSDAB topology schematic.**

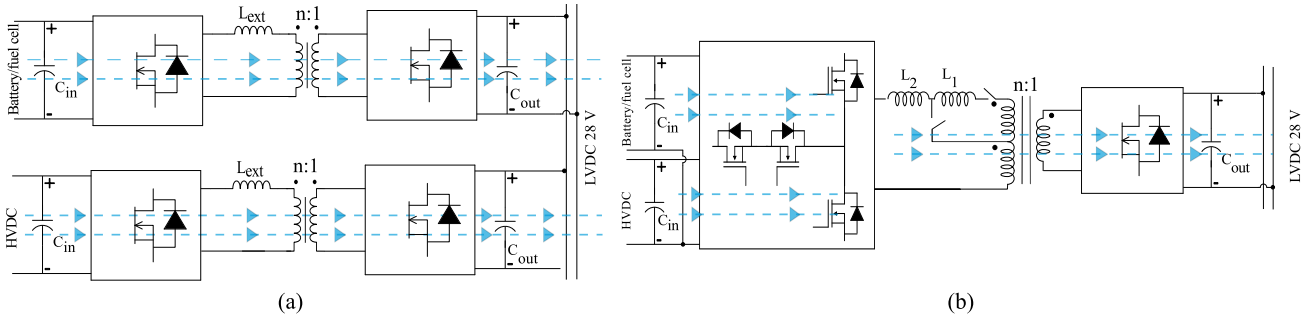

FIGURE 4. **DC/DC converters configuration. (a) Conventional dual converters configuration. (b) Single multi-source configuration**

had access to the same converters forming a multi-source architecture.

The different paralleled multi-source converters can be controlled by the main supervisor in a similar manner to the MPECs approach. Additionally, the power flow between the different sources can be controlled as well through the multi-source topology. Constant power needs to be supplied to the LV network and hence in case of voltage sag of any of the connected sources, a higher current is drawn to fix the delivered power which affects the system stability. In case of a voltage sag of the HVDC link, the power delivered from the HVDC link can be reduced and batteries, fuel cells as well as the APU can provide more power through the multi-source converter. The batteries can be used as well to regulate the HVDC voltage by controlling the multi-source converter as a boost converter which will be explained in Section II. B. The distribution system can be further optimized by determining the number of multi-source converter cells to be paralleled and investigating how the sources will be distributed among the cell terminals while considering the power supplied by each source.

A. Multi-source dual active bridge (MSDAB) converter structure vs. conventional DAB configuration

The DAB converter is the most commonly used converter topology in MEA application. This is due to the features offered by the DAB converter, such as high efficiency, zero voltage switching capability, and controllability. The topology is shown in Fig. 3 (a), where an inductor (L_{ext}) is added between the HV bridge and the isolating transformer known as the external leakage inductor. The operating principle of the converter is discussed in detail in [13], [14]. A multi-source derivative of the DAB converter is proposed in this paper and is shown in Fig. 3 (b).

Conventionally, each DC-DC converter is connected to the two HVDC links generated from the two main engines, or the APU HVDC link have to be sized at the rated power which results in an oversized system. Fig. 4 shows the conventional configuration of the DC-DC converters in the MEA architecture vs. the proposed multi-source structure. Fig. 4 (a) shows two converters that are supplied by a separate source and rated at full power. Alternatively, as shown in Fig. 4 (b), a single MSDAB can be used with two sources connected at the input side. Two lower power input-parallel-output-parallel (IPOP) converter units of the MSDAB can be considered to realize the MPECs structure allowing power split between the two sources. The modular parallel approach provides control flexibility and increased system reliability. The MSDAB delivers the same power as the two paralleled conventional converters preventing over-sizing of the distribution network. Two energy sources, the HVDC link, and the auxiliary 300 V battery/fuel cell are considered in this paper to illustrate the operating principle of the multi-source topology. Considering different voltage levels for the connected sources, the transformer turns ratio can be actively changed based on the operating mode. This is achieved by adding a tap changer to the transformer where some of the transformer turns can be bypassed in case of a lower input voltage. As shown in Fig. 3 (b), there is an additional switch added to the conventional topology, labelled S_9, which bypasses some of the transformer turns as well as part of the added external inductance. S_{10} is also added to avoid shorting the transformer during the battery mode. Both S_9 and S_{10} can be realized using a double pole double throw relay (DPDT) relay. Since the two switches are either on or off, no modulation is required for them and relays can be used to lower the number of required gate

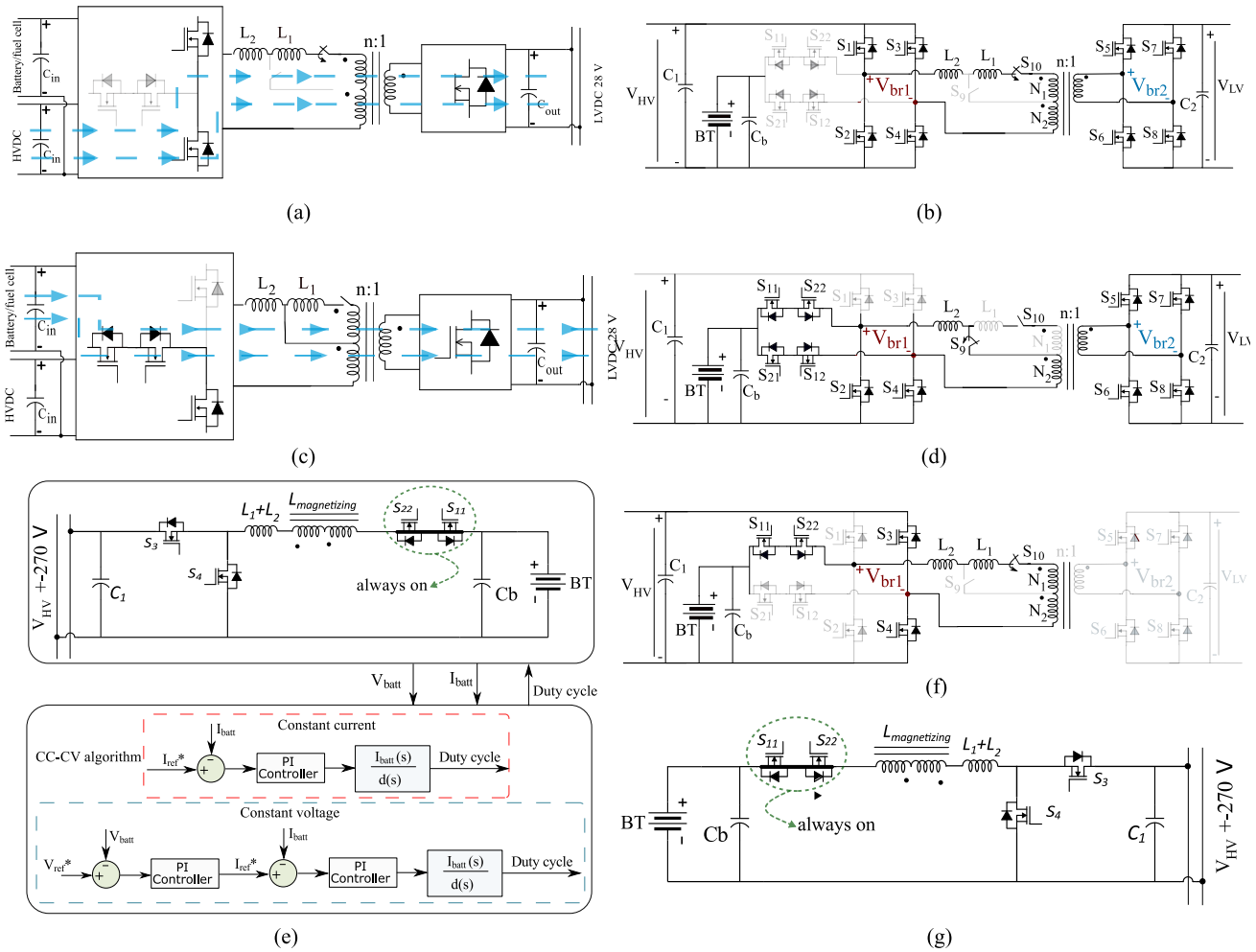

FIGURE 5. MSDAB modes of operation. (a) HVDC mode block diagram, (b) HVDC mode schematic, (c) battery mode block diagram, (d) battery mode schematic, (e) battery charging CC-CV technique, (f) battery charging mode schematic, and (g) bus regulation mode.

drivers, avoid a thermal management system and reduce the control complexity. This is added to have different optimized turns ratios and external inductance for each of the input sources. Power split between the two sources is achieved as well with the proposed structure. Two bidirectional switches are added to connect the second source to the primary side winding terminals. A switch (S_9) is placed across a portion of the primary transformer winding (N_1) to actively control the turns ratio. The placed switch (S_9) also bypasses a portion of the external inductance (L_1) for optimized ZVS operation in different operating modes. The transformer is configured as having a center-tapped winding on the primary side. The reason for the center-tapped configuration is that the HVDC bus voltage (540 V_{dc}) is almost twice the battery voltage (300 V), so that the converter would not be optimal if the same turns ratio and external inductance are used for both sources.

The cost highly depends on the system architecture and how many parallel units are considered. In the case of more parallel low-power cells which is the case of the MCPECs architecture presented in the paper, the proposed topology offers the advantage of reduced cost since the number of required converters in parallel is reduced as compared to the conventional structure.

B. Multi-source Dual Active Bridge (MSDAB) Modes of Operation

There are four main operating modes for the proposed converter; mode 1: supplying power to the LV network through the HVDC link, mode 2: supplying power from the battery/fuel cell (source 2) to the LV network, and mode 3: regulating the HVDC bus voltage in case of voltage sag by controlling the power flow from the battery to the HVDC bus, and mode 4: charging the battery from the HVDC bus. In each mode, the converter switches are modulated to control the power flow in the required direction. The control flexibility of such a system is improved as compared to the conventional structure since the power can be controlled

TABLE 1. Topology comparison - proposed MSDAB vs conventional DAB

Topology comparison		Devices		Magnetics	
		# Switches	Switch rating	# External inductors	# Transformers
Proposed MSDAB	Primary	10 (or 8 +2 relays)	V_{HV} * I_{HV}	2	1 (tap changer- using contactors)
	Secondary	4	V_{LV} * I_{LV}		
Conventional	Primary	8	V_{HV} * I_{HV}	2	2
	Secondary	8	V_{LV} * I_{LV}		

between the sources as well as the power supplied to the LV network. For the proposed structure, only one mode can be achieved at a time; for this reason, a lower-power paralleled converter is beneficial since each converter can be controlled by the main supervisor to provide power in the required direction.

The LV network can be supplied from the HVDC bus by turning off the additional bidirectional switches (S_{11}, S_{22}, S_{21}, and S_{12}), added for the second source. All transformer turns ($N_1 + N_2$) are utilized in that case to step down the HV to the lower voltage side. The generalized diagram of the HVDC mode is illustrated in Fig. 5 (a). The switching scheme of this mode is shown in Fig. 5 (b). The second mode of operation, shown in Fig. 5 (c), is when the converter is supplied from the battery. This is achieved by activating the two added bidirectional switches as well as the switch across a portion of the transformer's primary windings (N_1) as illustrated in Fig. 5 (d). This configuration is similar to the conventional DAB topology, and the same control principles of the DAB converter can be applied to control the power flow to the LV side. The bidirectional switches (S_{11}, S_{22} and S_{21}, S_{12}) are added to prevent the power flow from the HVDC link to the second source. Since the voltage is higher for the HVDC link than that of the battery, if a single switch is added, power will flow between the two sources through the body diode of the FETs. MIL-STD-704 mandates that blocking diodes must be added in case of using different DC power sources in parallel, which is the case in the proposed structure. For these reasons, an additional power switch is added in a bidirectional manner for protection. As illustrated, both the transformer turns ratio and added external inductance in the HVDC mode are higher than in the battery mode, since the bypassing switch is off. This comes from the requirement for a higher stepping-down ratio in the case of the HVDC operation. Furthermore, a split-power mode can be achieved by having two low-power converters in parallel where each is connected to an MSDAB converter.

Either both converters are supplied from the HVDC/battery, or power is split between the two sources through both converters. The MSDAB converter has two additional modes that are not possible with the conventional approach: bus regulation mode and battery charging mode. The battery charging mode is when power is supplied from the HVDC link to the battery. A conventional CC-CV charging algorithm can be implemented as shown in Fig. 5 (e), where the magnetizing inductance along with the added external inductance is utilized as a filter. The switching scheme of the battery charging mode is illustrated in Fig. 5 (f), where the converter is modulated as a buck converter. The proposed MSDAB can increase the stability of the system in the case of a voltage sag in the HVDC bus, where the battery is used to stabilize the bus voltage. In this case, the same switches as in the battery charging mode are used as shown in Fig. 5 (g). In this case, the converter is configured as a boost converter and the magnetizing inductance along with the external inductor are used as a filter. The battery charging and the bus regulation modes eliminate the conventional need of an additional external circuitry to perform bus stabilization or battery charging. Having multiple parallel low-power MSDAB converters allows for more flexibility for the controller to select different modes for each converter. Where some converters will permit power split between the two sources and other converters can be used for bus stabilization in case of voltage sag. It should be noted that power split refer to power sharing between different converter units not inside a single converter unit.

C. Design comparison: proposed MSDAB vs conventional DAB

Table 1 compares the conventional DAB solution and the proposed MSDAB topology in terms of the number of switching devices utilized in each, added external inductors, and the number of transformers. The device ratings of the primary side are normalized to the primary switch ratings of the conventional DAB converter. The number of secondary devices for the MSDAB is half of that of the conventional DAB topology, which is considered a major advantage for the MSDAB considering the design complexity and efficiency of the secondary high-current side. Less number of magnetic components are utilized for the MSDAB resulting in a higher power density as compared to the conventional solution.

III. MSDAB Converter Design and Optimization

This section goes through the design and control optimization process of the proposed MSDAB converter. The process is split into two optimization layers; the first is to determine the values of N_1, N_2, L_1, and L_2 shown in Fig. 5 (b). The second optimization layer is to determine the values of the optimized phase angles at several operating points for both the HVDC and battery operating modes. The angle

optimization is carried out based on the triple-phase-shift (TPS) control technique.

A. MSDAB converter modelling

The optimization process is based on a developed generalized model for the DAB converter based on the Fourier transform. There are several control techniques presented in the literature for the DAB converter. The simplest control technique for the DAB converter is phase-shift control where signals for both primary and secondary switches are phase-shifted, with a fixed 50% duty cycle, controlling the power flow in either direction [15]. Several DAB control techniques have been introduced in literature based on phase shifting the signals fed to the primary and secondary bridge legs [12], [16], [17]. The proposed modelling and optimization algorithm is based on the triple phase shift technique, which can be considered a generalized modulation technique for the DAB converter.

The MSDAB converter configuration in the two main modes, where power is supplied to the LV network from either the HVDC bus (HVDC mode) or from the battery (battery mode), can be simplified as shown in Fig. 6. The MSDAB converter in these two modes acts as the conventional DAB converter; however, with different switching devices being modulated in each mode as illustrated in Fig. 5 (b) and (d). The main differences between the two modes are: having a different input source connected at the input side, different external inductance, and transformer turns ratio for each mode. The DAB converter operation relies on the DAB inductor to transfer power in a bidirectional manner. The primary and secondary bridges can be modeled as two square-waveform generators on both sides of the inductor. The basic converter waveforms are shown in Fig. 6 for the TPS control algorithm. The inductor current can be formulated through the simplified MSDAB model as follows:

$$i_L = \frac{(V_{br1} - NV_{br2})}{Z_L}, \tag{1}$$

where V_{br1} is the primary bridge voltage, N is the primary to secondary transformer turns ratio, V_{br2} is the secondary bridge voltage, and Z_L is the inductor impedance. The Switching waveforms of V_{br1} and V_{br2} can be expressed as follows,

$$V_{br1}(\theta) = \begin{cases} V_{\text{in}}, & 0 < \theta < \phi_1 \\ 0, & \phi_1 < \theta < \pi \\ -V_{\text{in}}, & \pi < \theta < (\pi + \phi_1) \end{cases}$$
$$V_{br2}(\theta) = \begin{cases} V_{\text{out}}, & \phi_2 < \theta < \phi_3 \\ 0, & \phi_3 < \theta < (\phi_2 + \phi_3) \\ -V_{\text{out}}, & (\phi_2 + \phi_3) < \theta < (\pi + \phi_3) \end{cases} \tag{2}$$

Where V_{in} is the converter input voltage, V_{out} is the output voltage on the LV side, and ϕ_1, ϕ_2 , and ϕ_3 are the phase angle as illustrated in Fig. 6.

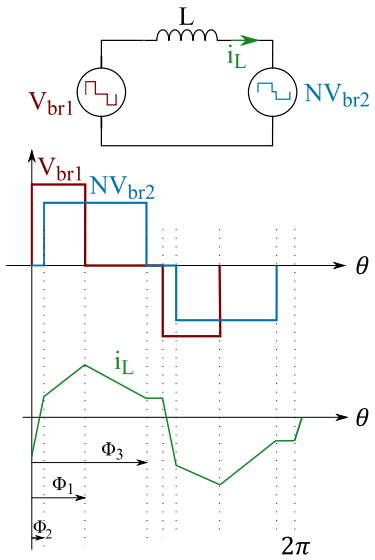

FIGURE 6. Simplified dual-active bridge model.

Both V_{br1} and V_{br2} can be expressed in the form of a Fourier expansion as in (3):

$$\mathrm{V}(\theta) = v_0 + \sum_{K=1}^{\infty} \left[v_{an} \cos(K\theta) + v_{bn} \sin(K\theta) \right], \tag{3}$$

where K is the harmonic order.

The bridge voltages, V_{br1} and V_{br2}, can be expressed in the expanded Fourier form as in (4):

$$V_{br1}(\theta) = \sum_{K=1,3,5,....}^{\infty} \frac{4V_{in}}{K\pi} \sin(\alpha) \cos(K\theta - \alpha)$$
$$V_{br2}(\theta) = \sum_{K=1,3,5,...,}^{\infty} \frac{4V_{out}}{K\pi} \sin(\beta) \cos(K\theta - \alpha - \epsilon), \tag{4}$$

where $\alpha = \dfrac{K\phi_1}{2}, \beta = \dfrac{K\left(\phi_3 - \phi_2\right)}{2}$, $\epsilon = K\phi_f$, and ϕ_f is the phase shift between the fundamental components of V_{br1} and V_{br2}.

By plugging (4) into (1), the inductor current can then be expressed as in (5):

$$i_L(\theta) = \sum_{K=1,3,5,...}^{\infty} \frac{2V_{in}}{K^2\pi^2 LF} [\sin(\alpha) \sin(K\theta - \alpha) - d \sin(\beta) \sin(K\theta - \alpha - \epsilon)], \tag{5}$$

where d is the converter gain and equals to $\dfrac{NV_{out}}{V_{in}}$, and F is the switching frequency.

The generalized inductor formula is used in the two-layer optimization algorithm. The algorithm objective is to minimize the RMS inductor current. Since the current on the LV network side is high, minimizing the RMS current is considered as the algorithm objective to optimize the efficiency. The RMS value of the inductor current is obtained numerically using MATLAB by implementing (5).

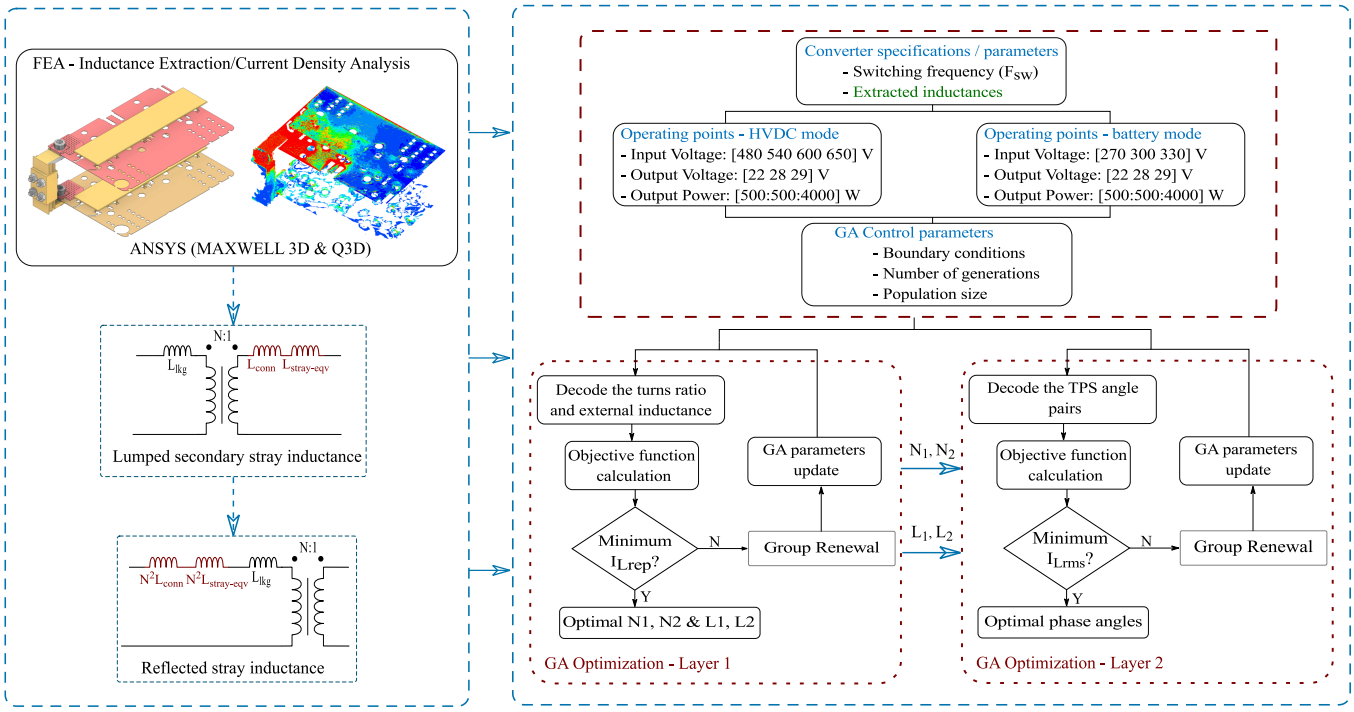

FIGURE 7. **Design methodology flow diagram - inductance extraction and GA optimization layers.**

TABLE 2. **CONVERTER SPECIFICATIONS**

Parameter	Value
HVDC voltage [V]	480 - 650
Battery voltage [V]	270 - 350
Output voltage [V]	22 - 29
Output power [kW]	4
Primary RMS current - HVDC mode [A]	10
Primary RMS current - battery mode [A]	20
Secondary RMS current [A]	220

The inductor current is a function of N, L_{ext}, and the three phase shift angles. Single phase-shift (SPS) is considered in the first layer of the optimization to select the optimal turns ratio and external inductor value for each operating mode separately.

B. MSDAB converter design and control optimization

The MSDAB converter specifications are listed in Table 2. Since the transition ratio between the HVDC bus to the LV bus is high, a transformer with a high turns ratio is required. The high turns ratio increases the effect of the stray inductance on the secondary side, altering converter operation. This is particularly important in high current converters, where multiple switches are connected in parallel, impacting current sharing. To ensure equal inductance and current sharing between paralleled branches, careful design of the connectors, layout, and PCB must be considered. The secondary inductance reflected on the primary side is proportional to the turns ratio squared. This reflected inductance varies for each mode of operation, due to differing turns ratio. Thus, obtainment of the external leakage inductance from an optimization algorithm is dependent on the reflected stray inductance. The optimization process is outlined in Fig (7). The stray inductance network can be represented as a single equivalent inductance shown in Fig. 7, connected in series with the connector inductance. Both inductances can then be reflected to the primary side. The total reflected inductance, which is a function of the turns ratio, is fed to the optimization algorithm.

The optimization process is split into two main layers. The first part includes optimization of the transformer turns ratio and external inductance, for the two main operating modes of the MSDAB. The second part optimizes the phase shift angle generating a look-up table (LUT) for different operating points under each mode. It is worth mentioning that the value of the reflected inductance is dependent on the transformer turns ratio which is an optimization variable in the algorithm.

As shown in Fig. 7, the stray inductance of the secondary side is extracted using ANSYS Q3D. A lumped total inductance is obtained to represent the total secondary side inductance. The lumped inductance is then reflected on the primary side. In each of the operating modes, this reflected inductance value is different due to the different turns ratio used in each mode. The N_1, N_2, L_1 and L_2 selection

is performed to minimize inductor RMS current across different operating points. The optimization is performed for both the HVDC and battery modes separately at various operating points. Different weighting factors are used for each point. Based on converter specifications, the weight of each operating point is determined. A representative RMS current for all operating points is analyzed. The operating range of the input and output voltages and the converter output power range are shown for the HVDC mode and battery modes.

$$V_{\text{in -HVDC}}(\text{i}) = \begin{pmatrix} 480\ \text{V} & 540\ \text{V} & 600\ \text{V} & 650\ \text{V} \end{pmatrix}$$
$$V_{\text{in - Battery}}(\text{i}) = \begin{pmatrix} 270\ \text{V} & 300\ \text{V} & 330\ \text{V} \end{pmatrix}$$
$$V_{\text{out}}(\text{j}) = \begin{pmatrix} 24\ \text{V} & 26\ \text{V} & 28\ \text{V} & 29\ \text{V} \end{pmatrix}$$
$$P_{\text{out}}(\text{k}) = \begin{pmatrix} 500\ \text{W} & 1\ \text{kW} & 2\ \text{kW} & 3\ \text{kW} & 4\ \text{kW} \end{pmatrix}$$

The representative RMS current, expressed in (6), is formed by summing out the RMS current of all points multiplied by the weighting factor set by the designer. This representative current is obtained separately for the HVDC and battery operations.

$$\bar{I}_{Lrms} = \sum_{i=1}^{4}\sum_{j=1}^{4}\sum_{k=1}^{5} W_{i,j,k} I_{rms}(i,j,k), \tag{6}$$

where $W_{i,j,k}$ is the weighting factor of the corresponding operating point.

The RMS current for each mode is evaluated based on the generalized formula derived in the previous section under SPS control, with the phase angle calculated according to (7) for all operating conditions.

$$P_{SPS} = \frac{NV_{in}V_{out}}{2LF}\phi_2(1-\phi_2), \tag{7}$$

where F is the switching frequency.

The lead inductances of all MOSFETs are the same. The series PCB stray inductance of the drain and source, which is reflected on the primary side, along with the lead inductances are added to the connector inductance. The extracted secondary side inductance is denoted as the equivalent inductance shown in Fig. 7. The optimization methodology is shown in Fig. 7, where the inductance values are extracted from ANSYS Q3D. The equivalent series inductance is fed to the optimization algorithm. A GA-based optimization is adopted to select the external inductor value and turns ratio. The GA process outputs an optimal solution by going through multiple generations and variable mutations. This optimization algorithm is simple and efficient and is therefore utilized in this paper. The following formulas linking the stray inductances to the turns ratio are used:

$$\begin{aligned} L_{\text{reflected}} &= N^2 L_{\text{stray-equivalent}} \\ L_{\text{total}} &= L_{\text{reflected}} + L_{\text{lkg}} + L_{ext}. \end{aligned} \tag{8}$$

The optimization problem of selecting N and L is defined as below:

$$\text{Min}: I_{rms} = \sum_{i=1}^{4}\sum_{j=1}^{4}\sum_{k=1}^{5} W_{i,j,k} I_{rms}(i,j,k)$$

Constraints:

$$L \le L_{\max},$$

where L_{max} is the maximum allowed inductance realizing all operating points. The maximum inductance is obtained at maximum input voltage and minimum power. The maximum allowable phase shift ($\phi_{\max}$) is $\pi/2$ to achieve maximum power for a given turns ratio and input voltage. The maximum inductance allowed is different in each operating mode and can be calculated using (9):

$$L_{max} = \frac{\phi_{\max}(\pi - \phi_{\max}) N V_{in-\max}}{2\pi F P_{\text{out-min}}}. \tag{9}$$

This condition ensures all operating points function under a maximum phase shift of $\pi/2$. After the selection of N and L_{ext}, the converter parasitics are considered. In this case study, the total stray inductance on the secondary side is obtained as 70 nH for the secondary side PCB and connectors. This value is fed to the N-L optimization layer of each operating mode referred to as "GA Optimization - Layer 1" in Fig. 7. The weighting factor ($W_{i,j,k}$) for the nominal point, mid-power level, and remaining power levels are 50%, 25%, and 25%, respectively. The weighting factor selection is based on the design requirements and the importance of each operating point. First, as shown in Fig. 8, the values of N (N_1 + N_2) and L (L_1 + L_2) are obtained, which are the turns ratio and inductance values utilized in the HVDC mode. After which, the values of N_2 and L_2 are obtained, which are the turns ratio and inductance values of the battery mode. Finally, the values of N_1 and L_1 can be attained. This corresponds to running the optimization algorithm twice to obtain the optimal turns ratio and inductance value of both main modes while having the same secondary inductance fed to the algorithm for both modes. The different turns ratio and inductance values utilized in each mode ensure optimal operation and a wider ZVS range of the MSDAB in the main two operating modes. The optimized values for the turns ratio and total inductance are 20:1 and 45 µH, 10:1 and 11 µH for the HVDC and battery mode respectively. Part of the resulting optimized inductance is the secondary reflected inductance. In this scenario, only 11 µH external inductance is needed in the HVDC mode and the remaining inductance is provided by the inherent secondary stray and connectors design and no external inductance is required for the battery mode. For this design case, L_2 = 0, L_1 = 11 µH. Both L_1 + N_1 are bypassed in the battery mode by turning on switch S_9 The N-L_{ext} selection is dependent on the hardware design and must be included in the optimization process.

The optimal values are inputted to the second GA optimization layer as demonstrated in Fig. 7. The objective of the second part of the optimization process is to find the optimal phase shift values, under TPS control.

The optimization process is repeated for all operating points. Unlike the first optimization layer where a single representative current is optimized, the individual operating points' current is optimized in the second part, with phase shift selection based on each operating point. The optimiza-

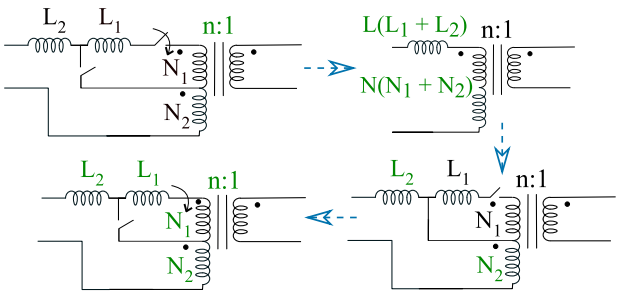

FIGURE 8. Optimization steps to attain the turn ratios and external inductances

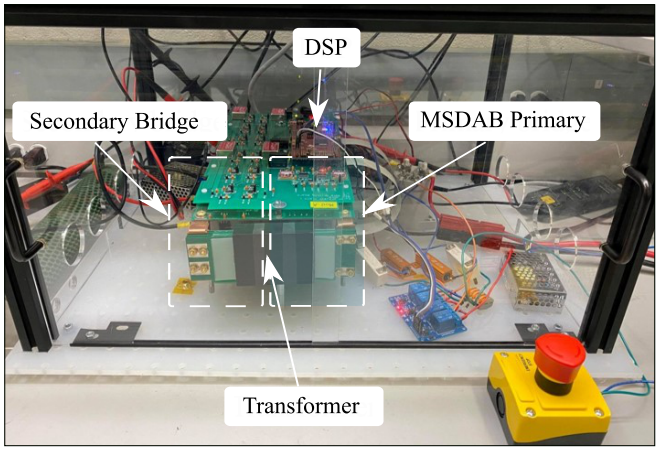

FIGURE 9. Multisource dual-active bridge experimental setup

tion process for the selection of the phase angles is defined as below: Min: $I_{\text{rms}}\left[\text{V}_{\text{in}}(i)\,\text{V}_{\text{out}}(j)\,\text{P}_{\text{out}}(k)\right]$

Constraints:

$$\phi_3 - \phi_2 \leq \pi$$
$$\phi_f < \frac{\pi}{2}$$
$$P = P_{avg},$$

where ϕ_f represents the phase shift between the fundamental components of the bridge voltages V_{ab} and V_{cd}. The first constraint is to ensure the maximum phase shift between the secondary legs is π which is the case for SPS modulation. The upper limit for ϕ_1 is set to π which restricts the phase shift between the primary legs to π. Similar to SPS, maximum power transfer occurs at $\phi_f = \pi/2$. This condition is a constraint, which is included in the optimization process. The final constraint ensures that the target power is obtained at the optimal phase angle.

IV. Experimental Validation

A 4-kW prototype, shown in Fig. 9, was built to validate the proposed MSDAB topology. The effectiveness of the proposed optimization methodology has been tested across different voltage and power levels in the main two operating modes. In the HVDC mode (HVDC link supplies power to the LV network), the transformer tap changer is deactivated and the full turns of the transformer are utilized to provide a high step-down ratio resulting from the optimization algorithm.

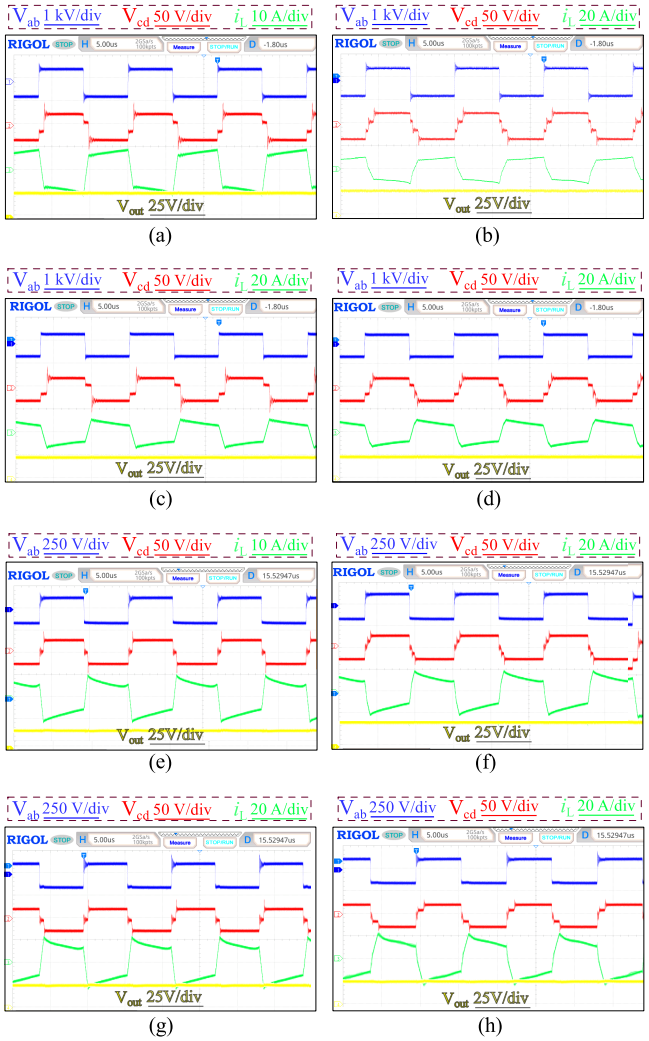

FIGURE 10. Experimental waveforms for SPS, TPS (N_1 = 9, N_2 = 11, $L_1 = 30\,\mu\text{H}$, $L_2 = 11\,\mu\text{H}$): (a) HVDC mode: SPS $V_{in}/V_{out} = 600/28$, (b) HVDC mode: TPS $V_{in}/V_{out} = 600/28$, (c) HVDC mode: SPS $V_{in}/V_{out} = 480/25.2$, (d) HVDC mode: TPS $V_{in}/V_{out} = 480/25.2$, (e) battery mode: SPS $V_{in}/V_{out} = 300/28$. (f) battery mode: TPS $V_{in}/V_{out} = 300/28$, (g) battery mode: SPS $V_{in}/V_{out} = 270/25.2$ and (h) battery mode: TPS $V_{in}/V_{out} = 270/25.2$

In the battery mode (battery supplies power to the LV network), the transformer ratio is adjusted using the tap changer to reduce the number of turns on the primary side since the input voltage is half that in the HVDC mode. ZVS is achieved through the added external inductor and the reflected stray inductance which is dependent on the turns ratio utilized in this mode. To validate the phase shift angles optimization, the converter is tested at multiple voltages and power operating points. The converter's power efficiency is measured for both operating modes under both SPS modulation and the optimized TPS angles. Fig. 10 shows key waveforms of the converter under the main two modes of operation, where the converter supplies power to

This article has been accepted for publication in IEEE Open Journal of Power Electronics. This is the author's version which has not been fully edited and content may change prior to final publication. Citation information: DOI 10.1109/OJPEL.2023.3256267

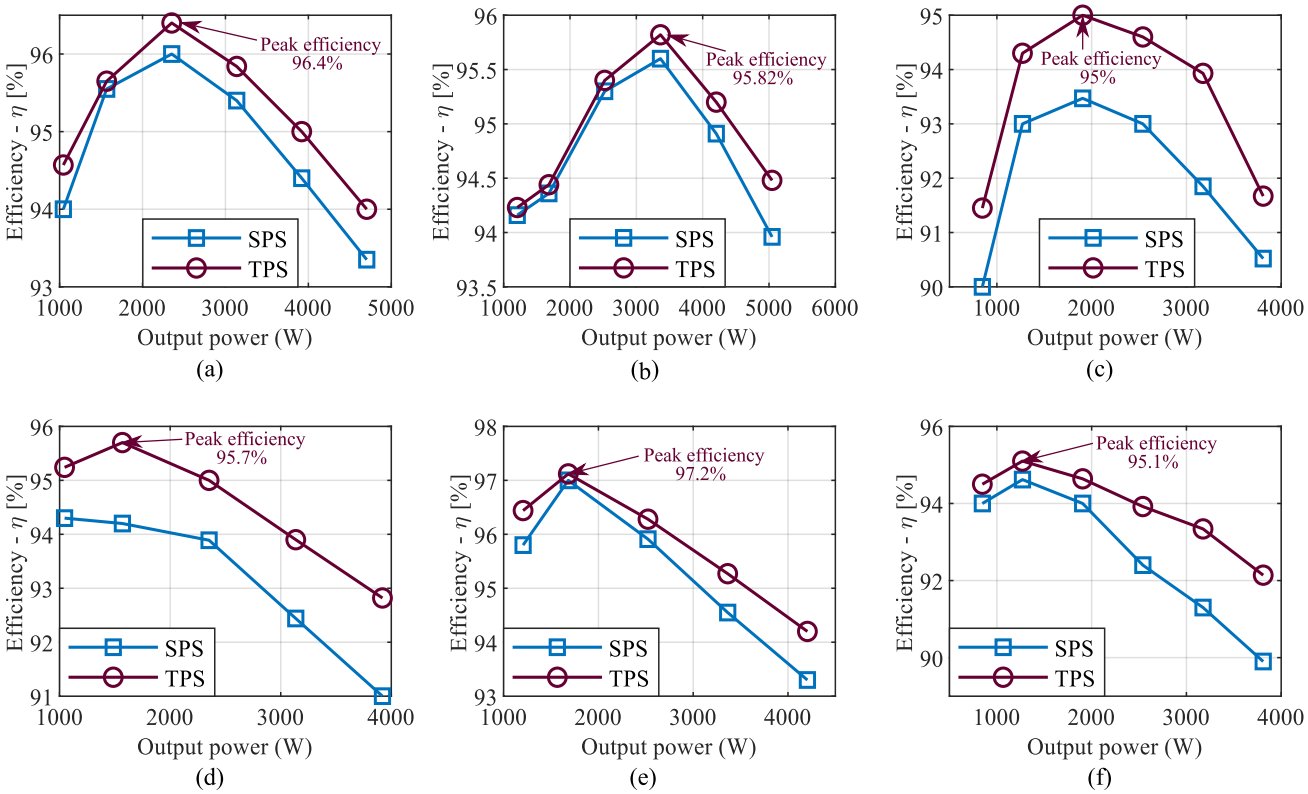

FIGURE 11. Experimental efficiency for SPS, TPS (N_1 = 9, N_2 = 11, $L_1 = 30\,\mu H$, $L_2 = 11\,\mu H$). (a) HVDC mode: $V_{in}/V_{out} = 600/28$. (b) HVDC mode: $V_{in}/V_{out} = 650/29$. (c) HVDC mode: $V_{in}/V_{out} = 480/25.2$, (d) battery mode: $V_{in}/V_{out} = 300/28$, (e) battery mode: $V_{in}/V_{out} = 330/29$, and (f) battery mode: $V_{in}/V_{out} = 270/25.2$.

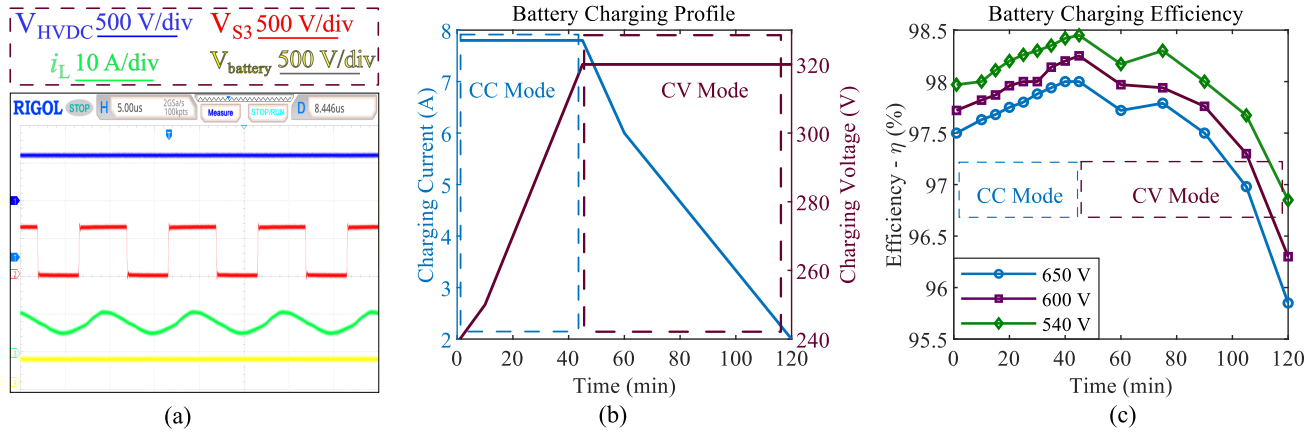

FIGURE 12. Experimental efficiency for the battery charging mode. (a) Converter waveforms at 2.5 kW, (b) battery CC-CV charging profile, and (c) Implemented charging profile using CC-CV technique at different input bus voltage

the LV bus. The extent of TPS optimization on the converter efficiency was tested at different power and voltage levels to highlight the effectiveness of the proposed optimization algorithm. The experimental efficiency plots for the two main modes are shown in Fig. 11. Different input and output voltage levels are considered, as shown in Fig. 11, to validate the developed algorithm across the whole converter operating range. For all the considered operating points in both operating modes, TPS modulation consistently outperformed the SPS modulation in efficiency. The third operating mode is when the converter operates so that the HVDC bus charges the battery.

The battery charging mode is then tested by modulating S_3 and S_4 as shown in Fig. 5(e). During this mode, the HVDC bus charges the battery, and the magnetizing inductance is utilized as a part of the output low pass filter. The measured magnetizing inductance of the transformer is 6.3 mH. The converter configuration in this mode is the same as the buck

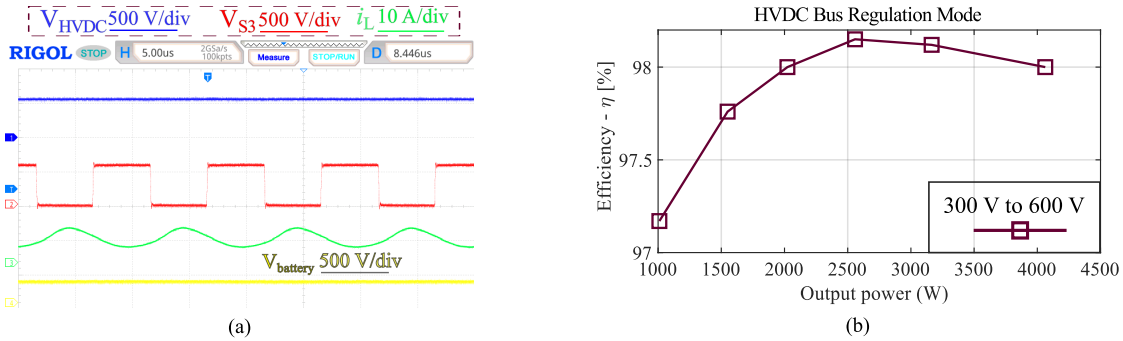

FIGURE 13. Experimental efficiency for the bus regulation mode: (a) Converter waveforms at rated 4 kW and (b) Converter efficiency at different power levels.

converter. An output capacitor is selected to be 150 µF to limit the voltage ripples to 0.5%. Two PI controllers are designed and implemented on the DSP C2000 Launchpad F28379D for the conventional CC-CV charging technique. The transfer functions of both the inner current loop and outer voltage loops are extracted using the small signal analysis toolbox in the PLECS environment. The charging power is limited to 2.5 kW in this mode, to extend the battery lifetime and prevent lithium plating due to high charging currents. The experimental waveforms of this mode are shown in Fig. 12 (a). The implemented charging profile is shown in Fig. 12 (b) and the experimental efficiency is plotted in Fig. 12(c) at different HVDC bus voltages. The efficiency of this operating mode is high across all operating points since only the HV side bridge is utilized.

Finally, the HVDC bus regulation mode is tested, where the battery (second source) supplies power to stabilize the HVDC link in case of voltage sag. Unlike the battery charging mode where the current is limited, the regulation current of the HVDC regulation mode can be set to the rated converter current. The experimental key waveforms of this mode are illustrated in Fig. 13 (a). The current waveform in Figure 12(a) and 13(a) is sinusoidal, instead of triangular, due to current probe bandwidth (100kHz) limitation. The main system-level supervisor sets the required current and power to stabilize the HVDC bus voltage. The converter is tested in this mode under different power demand conditions and the efficiency plot is shown in Fig. 13 (b).

V. Conclusion

In this paper, a MSDAB topology was proposed and different modes of operations for the converter were discussed showing the switching scheme for each mode. The topology allows for integration between two different sources to supply the LV network aboard the aircraft. The different modes add flexibility to the system, enabling power flow control between different sources in the EDPS of the aircraft. Better system utilization as compared to conventional solutions is achieved. The power density of the proposed MSDAB configuration is increased by the reduction in the number of switching devices as well as magnetic components. The MSDAB has been modeled based on the Fourier transform technique. A two-layer GA-based optimization process has been developed for the two main modes of the MSDAB topology. The algorithm was validated experimentally across different operating points and at various operating voltages. The efficiency considering the developed GA algorithm is improved by 1-2 % compared to the conventional SPS modulation technique. Furthermore, the power flow control between the two sources has been validated at different power levels. The proposed topology showed promise in terms of sources integration and system stability as compared to the conventional DAB converters often utilized in such applications.

Acknowledgment

The authors are particularly grateful for the technical assistance given by Lea Dorn Gomba from Enedym Inc., and Mario F. Cruz and Dr. Armen Baronian from EATON Aerospace Group.

REFERENCES

[1] P. Wheeler and S. Bozhko, "The more electric aircraft: Technology and challenges." *IEEE Electrification Magazine*, vol. 2, no. 4, pp. 6–12, 2014.

[2] G. Buticchi, L. Costa, and M. Liserre, "Improving system efficiency for the more electric aircraft: A look at dcdc converters for the avionic onboard dc microgrid," *IEEE Industrial Electronics Magazine*, vol. 11, no. 3, pp. 26–36, 2017.

[3] J. Chen, C. Wang, and J. Chen, "Investigation on the selection of electric power system architecture for future more electric aircraft," *IEEE Transactions on Transportation Electrification*, vol. 4, no. 2, pp. 563–576, 2018.

[4] "Airbus Wins, VoloCopter Debuts At GreenTec Awards," September 2013. [Online]. Available: https://www.avweb.com/news/airbus-wins-volocopter-debuts-at-greentec-awards/

[5] "Clean Sky 2: Programme overview and structure," October 2021. [Online]. Available: https://www.clean-aviation.eu/index.php/clean-sky-2/programme-overview-and-structure

[6] A. Chekin, Y. Moroshkin, K. Gubernatorov, and M. Kiselev, "Impact of reliability of state-of-the-art electrical units on architecture of power supply system of modern aircraft," in *2019 International Conference on Electrotechnical Complexes and Systems (ICOECS)*, 2019, pp. 1–6.

[7] B. Karanayil, M. Ciobotaru, and V. G. Agelidis, "Power flow management of isolated multiport converter for more electric aircraft," *IEEE Transactions on Power Electronics*, vol. 32, no. 7, pp. 5850–5861, 2017.

[8] H. Tao, A. Kotsopoulos, J. Duarte, and M. Hendrix, "Family of multiport bidirectional dc-dc converters," *Electric Power Applications, IEE Proceedings* -, vol. 153, pp. 451 – 458, 06 2006.

[9] G. Buticchi, S. Bozhko, M. Liserre, P. Wheeler, and K. Al-Haddad, "On-board microgrids for the more electric aircraft—technology review," *IEEE Transactions on Industrial Electronics*, vol. 66, no. 7, pp. 5588–5599, 2019.

[10] S. S. Muthuraj, V. K. Kanakesh, P. Das, and S. K. Panda, "Triple phase shift control of an lll tank based bidirectional dual active bridge converter," *IEEE Transactions on Power Electronics*, vol. 32, no. 10, pp. 8035–8053, 2017.

[11] J. Huang, Y. Wang, Z. Li, and W. Lei, "Unified triple-phase-shift control to minimize current stress and achieve full soft-switching of isolated bidirectional dc–dc converter," *IEEE Transactions on Industrial Electronics*, vol. 63, no. 7, pp. 4169–4179, 2016.

[12] A. K. Bhattacharjee and I. Batarseh, "Optimum hybrid modulation for improvement of efficiency over wide operating range for triple-phase-shift dual-active-bridge converter," *IEEE Transactions on Power Electronics*, vol. 35, no. 5, pp. 4804–4818, 2020.

[13] J. Walter and R. De Doncker, "High-power galvanically isolated dc/dc converter topology for future automobiles," in *IEEE 34th Annual Conference on Power Electronics Specialist, 2003. PESC '03.*, vol. 1, 2003, pp. 27–32 vol.1.

[14] A. Tong, L. Hang, G. Li, X. Jiang, and S. Gao, "Modeling and analysis of a dual-active-bridge-isolated bidirectional dc/dc converter to minimize rms current with whole operating range," *IEEE Transactions on Power Electronics*, vol. 33, no. 6, pp. 5302–5316, 2018.

[15] N. Noroozi, A. Emadi, and M. Narimani, "Performance evaluation of modulation techniques in single-phase dual active bridge converters," pp. 410–427, 2021.

[16] M. Kim, M. Rosekeit, S.-K. Sul, and R. W. A. A. De Doncker, "A dual-phase-shift control strategy for dual-active-bridge dc-dc converter in wide voltage range," pp. 364–371, 2011.

[17] C. Calderon, A. Barrado, A. Rodriguez, P. Alou, A. Lazaro, C. Fernandez, and P. Zumel, "General analysis of switching modes in a dual active bridge with triple phase shift modulation," *Energies*, vol. 11, no. 9, 2018.

Mohamed I. Hassan(Student Member, IEEE) received his B.S. degree in Electrical Engineering from Ain Shams University, Cairo, Egypt in 2018. In January 2019, he continued on to pursue his Master of Science degree in electrical and computer engineering with McMaster University focusing on power electronics converters. At the beginning of his studies at McMaster University, he joined the McMaster Automotive Research Center (MARC) research group where he worked on developing power-dense power electronics converters for aerospace applications. Mohamed is currently pursuing the Ph.D. degree with McMaster University, focusing on development of power electronics DC-DC converters.

Niloufar Keshmiri(Student Member, IEEE) received the B.Eng. and Management degree in 2018, in electrical engineering and management from McMaster University, Hamilton, ON, Canada, where she is currently working toward the Ph.D. degree with the McMaster Automotive Resource Centre, Hamilton, ON, Canada. Her research focuses on the application of GaN wide bandgap devices in power electronics DC-DC converters for electrified transportation applications.

Omar Zayed(Student Member, IEEE) received the B.Sc. degree in mechatronics engineering from Ain Shams University, Cairo, Egypt in 2019. In 2020, he continued to pursue a M.Sc. degree in the electrical and computer engineering department at McMaster University, Hamilton, ON, Canada. Where he focused on power electronics converters. Omar is currently working toward a Ph.D. degree at McMaster University, focusing on research and development of power electronic converters. Which include: development of DC/DC converter for universal EV ultra-fast chargers at the high-power electronics lab (HiPEL) at McMaster, and multi-level medium voltage motor drives for industrial applications.

M. Narimani(Senior Member, IEEE) received the Ph.D. degree in electrical engineering from the University of Western Ontario, London, ON, Canada, in 2012. He is currently an Associate Professor with the Department of Electrical and Computer Engineering, and University Scholar at McMaster University, Hamilton, ON, Canada. He also holds the NSERC Canada Research Chair (CRC) position in high power converter systems. Prior joining McMaster University, he was a Power Electronics Engineer with Rockwell Automation Canada, Cambridge, ON, Canada. He has authored/coauthored more than 150 journal and conference proceeding papers, co-authored a Wiley-IEEE Press book, and holds 8 issued/pending US/European patents. He has been Associate Editor for IEEE Transactions on Power Electronics, IEEE Transactions on Vehicular Technology and vice chair and topic char for top tier conferences such as IEEE Energy Conversion Congress and Exposition (IEEE ECCE) and IEEE Applied Power Electronics conference and Exhibition (IEEE APEC). His current research includes power conversion, control of power electronics converters, fast EV Chargers, and wireless EV charging systems.

Ali Emadi(IEEE S'98-M'00-SM'03-F'13) received the B.S. and M.S. degrees in electrical engineering with highest distinction from Sharif University of Technology, Tehran, Iran, in 1995 and 1997, respectively, and the Ph.D. degree in electrical engineering from Texas A&M University, College Station, TX, USA, in 2000. He is the Canada Excellence Research Chair Laureate at McMaster University in Hamilton, Ontario, Canada. He is also the holder of the NSERC/FCA Industrial Research Chair in Electrified Powertrains and Tier I Canada Research Chair in Transportation Electrification and Smart Mobility. Before joining McMaster University, Dr. Emadi was the Harris Perlstein Endowed Chair Professor of Engineering and Director of the Electric Power and Power Electronics Center and Grainger Laboratories at Illinois Institute of Technology in Chicago, where he established research and teaching facilities as well as courses in power electronics, motor drives, and vehicular power systems. He was the Founder, Chairman, and President of Hybrid Electric Vehicle Technologies, Inc. (HEVT) - a university spin-off company of Illinois Tech. Currently, he is the President and Chief Executive Officer of Enedym Inc. and Menlolab Inc. - two McMaster University spin-off companies. He is the principal author/coauthor of over 500 journal and conference papers as well as several books including Vehicular Electric Power Systems (2003), Energy Efficient Electric Motors (2004), Uninterruptible Power Supplies and Active Filters (2004), Modern Electric, Hybrid Electric, and Fuel Cell Vehicles (2nd ed, 2009), and Integrated Power Electronic Converters and Digital Control (2009). He is also the editor of the Handbook of Automotive Power Electronics and Motor Drives (2005) and Advanced Electric Drive Vehicles (2014). He is the co-editor of the Switched Reluctance Motor Drives (2018). Dr. Emadi was the Inaugural General Chair of the 2012 IEEE Transportation Electrification Conference and Expo (ITEC) and has chaired several IEEE and SAE conferences in the areas of vehicle power and propulsion. He was

the founding Editor-in-Chief of the IEEE Transactions on Transportation Electrification from 2014 to 2020.